Impacts of El Niño and La Niña on interannual snow accumulation in the Andes: results from a high-resolution 31-year reanalysis

Article *in* Geophysical Research Letters · June 2017

DOI: 10.1002/2017GL073826

CITATIONS
3

READS
112

2 authors, including:

Gonzalo Cortés
University of California, Los Angeles
22 PUBLICATIONS **244** CITATIONS

SEE PROFILE

AGU PUBLICATIONS

Geophysical Research Letters

RESEARCH LETTER
10.1002/2017GL073826

Key Points:
- Using data assimilation, retrospective high-resolution SWE estimates were generated over the extratropical Andean region
- SWE over the Andes shows significant temporal variability and a marked contrast between western and eastern watersheds
- El Niño plays a significant positive role in deep snow accumulations; however, the effects of La Niña in SWE are not as clear

Supporting Information:
- Supporting Information S1

Correspondence to:
G. Cortés,
gcortes@ucla.edu

Citation:
Cortés, G., and S. Margulis (2017), Impacts of El Niño and La Niña on interannual snow accumulation in the Andes: Results from a high-resolution 31 year reanalysis, *Geophys. Res. Lett.*, *44*, doi:10.1002/2017GL073826.

Received 17 APR 2017
Accepted 13 JUN 2017
Accepted article online 16 JUN 2017

Impacts of El Niño and La Niña on interannual snow accumulation in the Andes: Results from a high-resolution 31 year reanalysis

Gonzalo Cortés[1] **and Steven Margulis**[1]

[1]Department of Civil and Environmental Engineering, University of California, Los Angeles, California, USA

Abstract We present new insights on extratropical Andean snow climatology (27°S to 37°S) based on the results from a 31 year high-resolution reanalysis. The snow water equivalent (SWE) estimates were generated by integrating observed snow depletion data from Landsat together with a snow model forced by the Modern-era Retrospective Analysis for Research and Applications. The spatial resolution (180 m), geographic extent (175,000 km^2), and temporal span (1984–2015) constitute an unprecedented data set for the region. SWE reaches annual peak volumes between 13 and 66 km^3, with a climatological average of 27.7 km^3. A positive correlation between SWE and the Oceanic Niño Index (R^2 = 0.35) exists for the region, with a strengthening of the signal from north to south, peaking at 34°S. Although the correlation between El Niño and positive SWE anomalies is significant, La Niña was not found to drive negative anomalies beyond what is observed during non-La Niña years.

Plain Language Summary This article presents a new data set of snow water resources over the Andes extratropical region of the countries of Chile and Argentina. The methods integrate Landsat satellite data with numerical models to derive an enhanced snow data set for a region where access to in situ snow measurements is limited due to geographical and logistical constrains.

1. Introduction and Objectives

The Andes is the most significant mountain range in the Southern Hemisphere in terms of elevation and extent, and it impacts the atmospheric circulation across scales ranging from the synoptic to the microscale, resulting in different phenomena that affect the hydrology of the entire South American continent [*Garreaud*, 2009]. Yet as in other mountain regions throughout the globe, many basic questions on Andean snowpack remain largely unanswered due to lack of data, and an observation-driven, continuous characterization of seasonal snow water volume and its temporal and spatial variability is still missing. Existing in situ networks over the region do not have a spatial density adequate enough to address small-scale (<1 km) features in snow accumulation, and forward modeling generally lacks sufficient accuracy over large scales due to relatively uncertain or biased input forcing data.

Dozier et al. [2016] describe the problem of characterizing the spatiotemporal distribution of SWE over mountain regions as one of the most important unsolved issues in snow hydrology. The Andean region represents an excellent example of the challenges that exist when addressing this problem due to the significant topographic complexity and influence of different climate regimes, which result in complex interactions leading to significant spatial variability across small scales [*Cortés et al.*, 2016]. Previous studies have attempted to better characterize SWE spatial variability and analyze trends using retrospective energy-based SWE reconstructions for the 2001–2014 period [*Cornwell et al.*, 2016], forward model simulations (4 km resolution, forced by Modern-era Retrospective Analysis for Research and Applications (MERRA) [*Mernild et al.*, 2016]), and regional indices derived from in situ data [*Masiokas et al.*, 2006]. We highlight these valuable data sets and the relevant science questions addressed by previous studies; however, the known biases of MERRA over the Andes [*Yi et al.*, 2011; *Cortés et al.*, 2016], the scarce in situ data, and biases in remotely sensed Moderate Resolution Imaging Spectroradiometer Snow Covered Fraction data [*Rittger et al.*, 2013] likely hinder the ability of such methods in capturing the complex spatial patterns of Andean snow at high resolutions (<500 m). The development of methodologies that combine high-resolution remotely sensed observational data sets together with robust modeling frameworks is necessary for the region, allowing the leveraging of the benefits of high-resolution observations over complex topography and adequately addressing the underlying uncertainty of the data sets through ensemble methods.

In this paper a new high-resolution snow data set for the Andes is presented. The methods used to generate it aim to mitigate some of the shortcomings mentioned above by integrating high-resolution remote sensing imagery and modeling within a data assimilation framework. The framework integrates an ensemble of snow model simulations forced by MERRA [*Rienecker et al*., 2011] together with Landsat fractional snow covered area (fSCA) data [*Margulis et al*., 2015] via Bayesian principles (i.e., data assimilation), combining the physics of a land surface model (LSM) with the information content from the remotely sensed Landsat data and the meteorological reanalysis forcing data. The method has been shown to be a robust generalization of retrospective energy-based reconstructions [*Girotto et al*., 2014] and has been used to characterize the long-term climatology of the Sierra Nevada and the recent effects of the 2011–2016 California drought [*Margulis et al*., 2015, 2016a, 2016b]. The generated estimates of snowpack states are consistent with the historical remotely sensed observed depletion record, explicitly taking into account the inherent uncertainties of all sources of the information used. In this work, we characterize the spatiotemporal distribution of SWE over the extratropical Andes, emphasizing conditions present during El Niño and La Niña years.

2. Methods

2.1. Study Area

The study domain (Figure 1a) consists of the extratropical Andes between 27°S and 37°S above 1500 mean annual sea level (i.e., the nominal snowline). The region represents the headwaters of the most important Chilean and Argentinean mountain watersheds (Pacific and Atlantic draining, respectively). The climate is alpine with a large spatial variability in precipitation, ranging from arid over the north (usually below 100 mm/yr) to the more humid south (above 2000 mm/yr). The highest temperatures are observed during the months of November to March (Spring-Summer season), which coincide with the driest months. The months of June–September (winter season) are characterized by lower temperatures and higher precipitation. The physiographic characteristics of each of the watersheds are tabulated in Table S1 in the supporting information.

2.2. Remote Sensing Data, Modeling, and Assimilation Framework

The methodology used in this study is presented in detail in *Margulis et al.* [2015, 2016a] and *Cortés et al.* [2016] and described in detail in Text S1 and Figure S1 in the supporting information. The methodology uses ensemble estimates of SWE and fSCA from forward modeling (prior) and then conditions them via data assimilation of historical fSCA data from Landsat TM, ETM+, and OLI sensors (totaling more than 5000 images). The assimilation step results in posterior SWE and fSCA estimates that are probabilistically conditioned on the observed depletion record from Landsat and on the forward model state uncertainty. The fSCA retrieval is performed using a spectral unmixing algorithm [*Painter et al*., 2003; *Cortés et al*., 2014].

The forward model used to generate the prior ensemble estimates is the SSiB3 LSM [*Yang et al*., 1997; *Xue et al*., 2003] combined with a Snow Depletion Curve model (SDC) [*Liston*, 2004]. LSM and SDC are used to generate the prior ensemble estimates of snowpack states at an hourly time step and at a resolution of 180 m. The ensemble forcing fields used as input for the LSM were generated by characterizing the MERRA uncertainty [*Girotto et al*., 2014] using the local meteorological observation network and then downscaling those fields to the 180 m resolution as described in Text S1 in the supporting information (downscaling of MERRA from the native resolution of 0.5° latitude by 2/3° longitude to the model grid of 180 m consisted of topographic adjustment of radiation, temperature, humidity and pressure) [*Kunkel*, 1989; *Cosgrove et al*., 2003; *Liston and Elder*, 2006; *Urrutia and Vuille*, 2009; *Girotto et al*., 2014; *Cortés et al*., 2016]. Precipitation uncertainty at each model grid cell was represented via a multiplicative error coefficient [*Pan et al*., 2003], characterized using the in situ meteorological network which is implicitly updated during the assimilation step.

The Particle Batch Smoother (PBS) data assimilation algorithm described by *Margulis et al.* [2015, 2016a] and further implemented over Andean test verification sites by *Cortés et al.* [2016] is used. In the PBS algorithm, the prior and posterior ensemble replicates are the same. For the prior ensemble, the prior weight associated with each replicate is the same: the assimilation step updates these weights based on the assimilated fSCA observations, assigning higher weights to those replicates that show model predictions closer to the observations (higher likelihood) and lower weights for those with larger differences (lower likelihood). The prior and posterior weights can then be used to calculate prior and posterior ensemble metrics such as the ensemble median SWE. Verification of the reanalysis framework results has

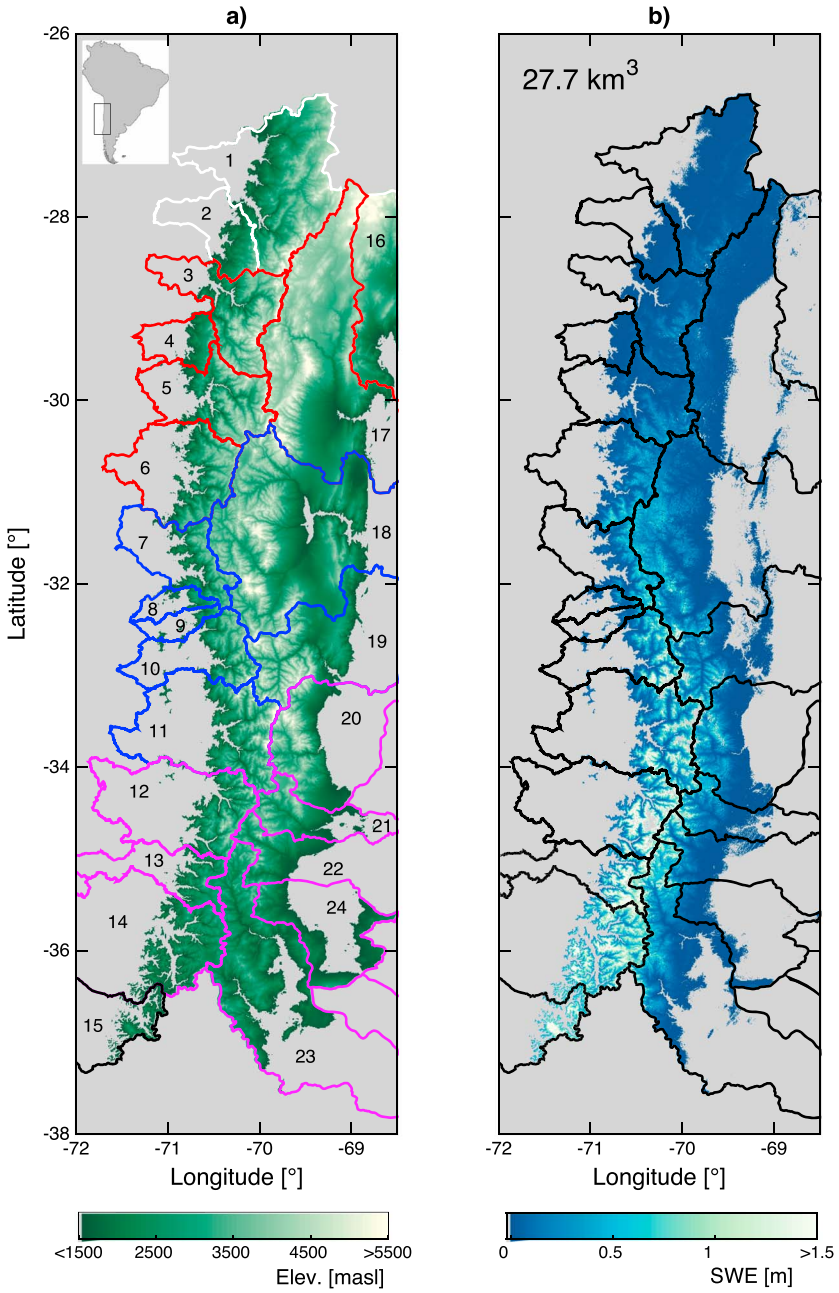

Figure 1. (a) Study domain showing the elevation and delineation of each of the watersheds (identified by basin IDs and cluster analysis categorization in Table S1); (b) 31 year average pixelwise peak SWE climatology.

been performed for the Sierra Nevada using in situ sensor data [*Margulis et al.*, 2016a] and for the Andes [*Cortés et al.*, 2016] using more than 2000 snow survey points obtained from 2009 to 2015 (Figure S2 in the supporting information) and 350 site years of peak annual snow pillow and snow course SWE data from 1985 to 2015. Verification results showed unbiased posterior estimates of SWE with a correlation coefficient of 0.73, RMSE of 0.29 m, and mean error of less than 0.01 m using snow pillow and snow course peak SWE. Results using snow survey data showed similar unbiased estimates as well with a correlation coefficient of 0.50, RMSE of 0.29 m, and mean error of less than 0.01 m. *Cortés et al.* [2016] found that no significant posterior error structure was found to exist as a function of elevation, slope, aspect, and wind exposure/sheltering. A more detailed analysis of the verification results is described in Text S1 in the supporting information, with the information for the verification sites tabulated in Table S3.

2.3. Spatiotemporal Analysis

The spatiotemporal distribution of SWE is analyzed herein by computing the water year (1 April to 31 March) annual peak SWE over each of the grid cells of the domain. The annual peak SWE corresponds to the maximum value observed during the water year for any given pixel (i.e., pixelwise peak). Hydrology of rivers within the region is characterized by a period of low flows from April to August, followed by an increase in streamflow due to melt of the snow, peaking between November and January. Previous work has shown a very high correlation ($>$0.90) between observed seasonal flows and in situ snow data [*Masiokas et al*., 2006]. A cluster classification [*Kaufman and Rousseeuw*, 2009; *Rubio-Álvarez and McPhee*, 2010; *Cornwell et al*., 2016] was performed using the integrated peak SWE volumes observed over each of the study watersheds in order to identify zones of long-term coherent behavior (see Text S3 in the supporting information). The impact of El Niño–Southern Oscillation (ENSO) is analyzed by evaluating the annual pixelwise peak SWE distribution during each of the El Niño and La Niña years that occurred during the 1984–2014 water years. Each year during which El Niño or La Niña conditions were present was classified according to strength (very strong, strong, and weak) using the Oceanic Niño Index (ONI) time series from NOAA (Table S1).

3. Results and Discussion

3.1. Spatial and Temporal SWE Distribution

Figure 1a shows the results of the cluster classification analysis by outlining the study watersheds that belong to the same cluster with the same color. The domain can be partitioned into five distinct snow accumulation zones: northern arid, northern semiarid, central semiarid, central Mediterranean, and southern. The classification is in general consistent between watersheds at both sides of the continental divides. We anticipate that a pixelwise cluster classification would result in less discrete borders between the zones, but the computational costs of performing such classification are significant given the large domain and high resolution. Figure 1b shows the pixelwise climatological value of peak annual SWE over the study period. The mean integrated pixelwise peak SWE over the domain was found to be approximately 27.7 km^3. The values presented here do not include snow over glacierized areas, where the reanalysis framework is not applied due to the lack of seasonal fSCA disappearance over the ice. Table S1 in the SI details the pixelwise peak SWE volumes for each of the watersheds over the domain. The spatial variation in SWE is a direct consequence of the latitudinal variation of precipitation between the arid Northern and humid Southern Andes, a feature widely documented by other authors [e.g., *Montecinos et al*., 2000; *Viale and Nuñez*, 2011], together with the variations in elevation across the domain. There is a significant contrast between SWE on the western (windward) and eastern (leeward) sides of the range due to orographic enhancement and rain shadow effects [*Viale and Nuñez*, 2011], with Pacific draining watersheds containing more than twice (19 versus 8.7 km^3) the climatological peak SWE volumes of the Atlantic draining watersheds despite having half the area (i.e., Pacific draining watersheds accumulate approximately 3.7 times more snow per unit area in comparison to Atlantic draining watersheds). The deepest SWE is observed between 33.5°S and 36°S, peaking at approximately 35.5°S where the effect of orographic enhancement, latitudinal precipitation bands, and elevation reaches a combined maximum.

Figure 2 shows the spatial patterns of annual peak SWE anomalies. Years with significantly higher SWE are generally related to El Niño occurrence (e.g., 1987, 1992, 1997, and 2002; see Table S2 in the supporting information). The driest years on record correspond to 1985, 1996, 1998, and the period 2010–2014, which is unprecedented in terms of drought duration and extent [*Boisier et al*., 2016]. The highest range-wide SWE occurred during 1987 (very strong El Niño year), with a total of approximately 66.3 km^3, while the lowest occurred during 1998 (strong La Niña year), totaling approximately 12.9 km^3.

We observed clear bimodal patterns of anomalies during years 1993, 1994, 1995, and 2009. For all of these years the latitudes north of 33–34°S show negative SWE anomalies, and south of this divide we observe positive SWE anomalies. For the rest of the years the anomaly signs are uniform throughout the domain. *Masiokas et al.* [2006] identify weakening of the subtropical Pacific anticyclone as a factor driving the positive anomalies in snow accumulation over a similar geographical domain. The results presented herein suggest that the consequence of this weakening is present throughout the entire extratropical Andes domain where snow is present, with only a few instances of bimodality observed throughout the time series. Similarly, *Viale and*

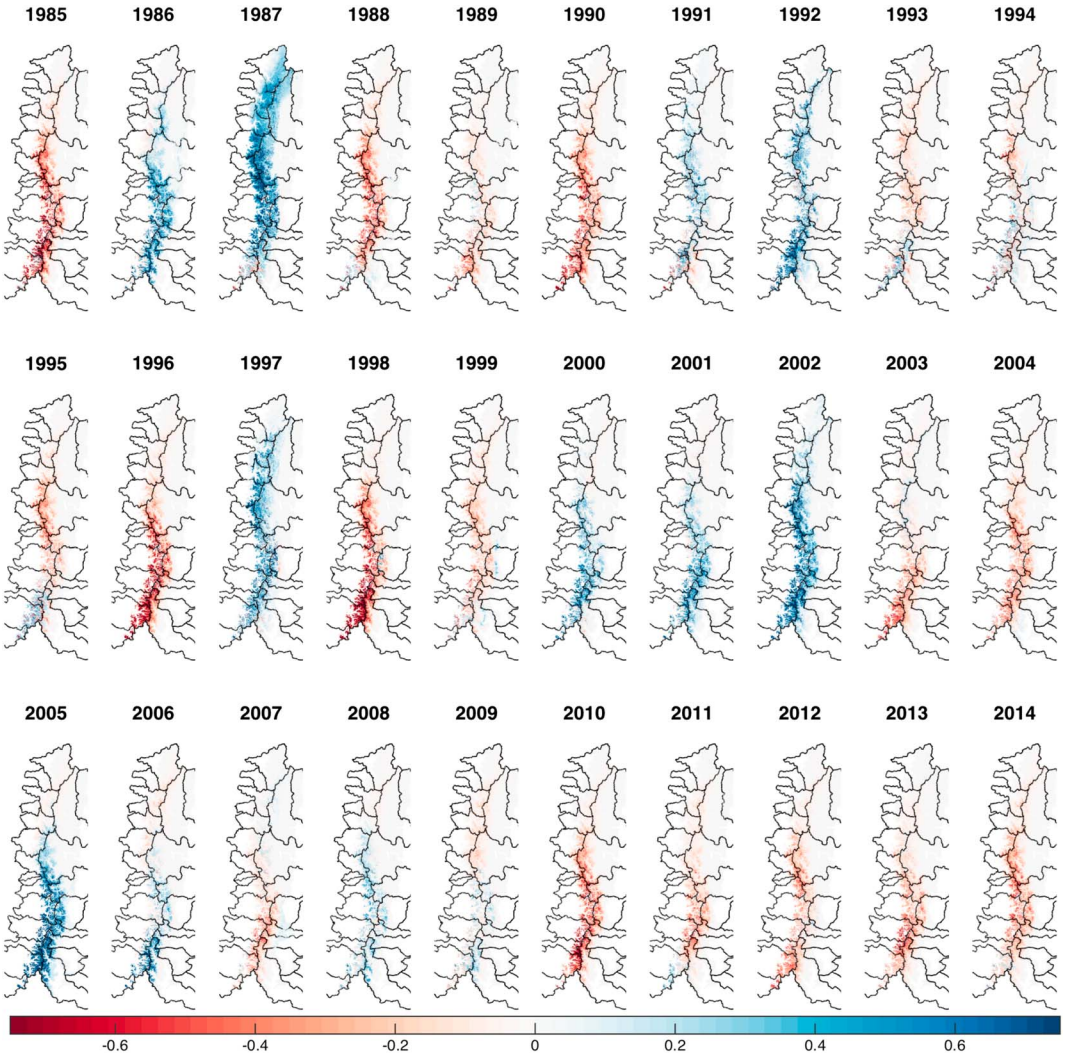

Figure 2. Annual pixelwise peak SWE anomaly (in meters).

Nuñez [2011] relate heavy precipitation events to strong water vapor transport from the Pacific. This transport is reduced with the strengthening of the Pacific Anticyclone, reducing the amount of moisture that reaches the Andes and hence SWE accumulation.

3.2. El Niño and La Niña Influence on Snow Accumulation

Figure 3 shows Hovmöller diagrams (latitude versus time) for annual peak SWE, together with the corresponding *Z* score (the value of the year minus the mean, divided by the standard deviation). The latitudinal SWE distribution was calculated by averaging all of the SWE values over 0.1° (approximately 10 km) latitude bins. The strongest positive anomalies generally occur during very strong and strong El Niño years. It is not possible to assert a strong correlation between La Niña years and negative SWE anomalies. The northern region (north of 30°S) is usually in a state of quasi-permanent snow drought, with *Z* score values generally negative and only interrupted by a few wet El Niño years. The last year with a predominant pattern of significant positive anomalies for the extratropical Andes was 2002, and the whole domain experienced snow-drought conditions between 2005 and 2015.

The pixelwise annual peak SWE maps averaged over the different years according to each ENSO classification are shown in Figures 4a–4e. The value for each pixel was calculated as the average of peak SWE values for the years belonging to each of the defined ENSO categories. There is a clear monotonic

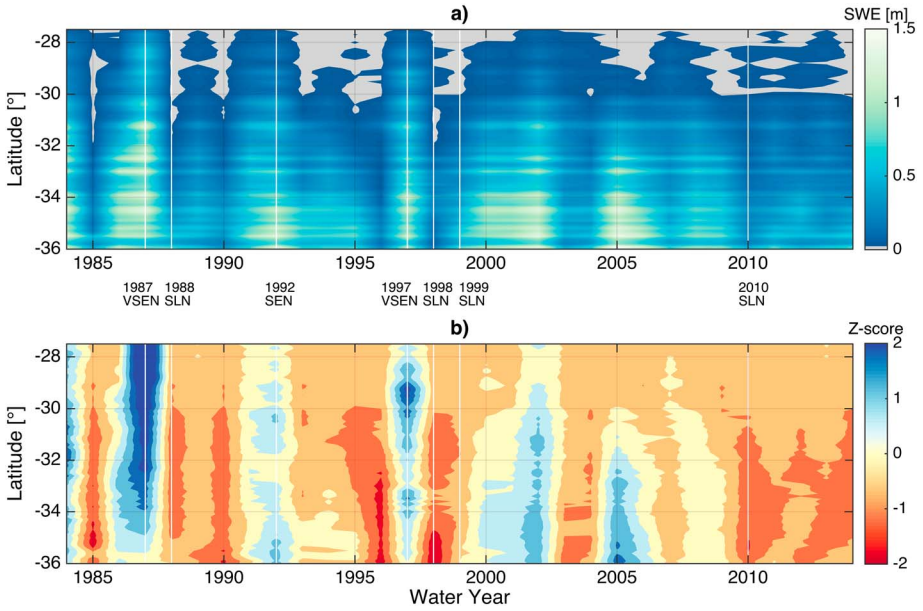

Figure 3. Hovmöller diagram for annual pixelwise peak (a) SWE distribution and corresponding (b) *Z* score. Very strong El Niño (VSEN), strong El Niño (SEN), and strong La Niña (SLN) years are identified.

pattern when the effect of ENSO in SWE is presented this way: El Niño years are generally wetter than La Niña years, and at a first glance the strength of the ENSO shows a direct influence to how wet or dry the average pattern is; however, these results need to be analyzed carefully as the relationship between ENSO and SWE is quite noisy (see Figure 5). The average integrated water volume during the two very strong El Niño years (65.1 km^3, 1987 and 1997) was nearly 5 times the average integrated water volume during the strong La Niña years (14.6 km^3), and more than twice the average water volume (30.3 km^3) over the 1984–2014 water years. There were no very strong La Niña years during the analyzed period according to the classification system used.

Figures 4f–4j show the Hovmöller diagrams for the latitudinal distribution of weekly averaged SWE during the years belonging to the different El Niño/La Niña categories (same years as Figures 4a–4e). During El Niño years, SWE shows high positive anomalies throughout the entire domain. The duration of the snow cover is also significantly higher than other years, ranging from approximately 30 weeks over the northern latitudes to more than 40 weeks over the southern regions (and even persisting beyond the end of the water year for some high-elevation locations). Figure 4j shows a significant snow presence during the beginning of the water year as two of the strong La Niña years (1988 and 1998) were preceded by a very strong El Niño. The persistent snow appears only to be relevant south of 32°S, and the northern latitudes show extremely low snow volumes and no year-to-year persistence of snow, even after the strong 1987 El Niño. During strong La Niña years, the snow cover duration is greatly diminished with respect to El Niño years: for the northern regions, there is minimal snow cover, lasting for only 10–20 weeks.

Figure 5a shows the latitudinal SWE distribution for each year analyzed, and Figure 5b shows the corresponding *Z* score value. This figure is similar in nature to Figure 3, with the difference that in here the information regarding ENSO fluctuations is conveyed by coloring each of the different latitudinal values according to the April–September ONI value for the water year. The values have been color coded according to the average ONI value during the year, with blue showing positive ONI values (El Niño conditions) and red showing negative ONI values (La Niña conditions). While wet years are usually associated with positive ONI values, only 1987 and 1997 stand out as significantly higher accumulations across the entire latitude range of the reanalysis. WY 1987 is particularly interesting as it is the only year that showed a wide difference (albeit same sign) between the anomalies observed in the northern latitudes and the southern latitudes, with the northern latitudes of the domain showing *Z* scores close to 5 for the arid regions north of 29°S. La Niña years

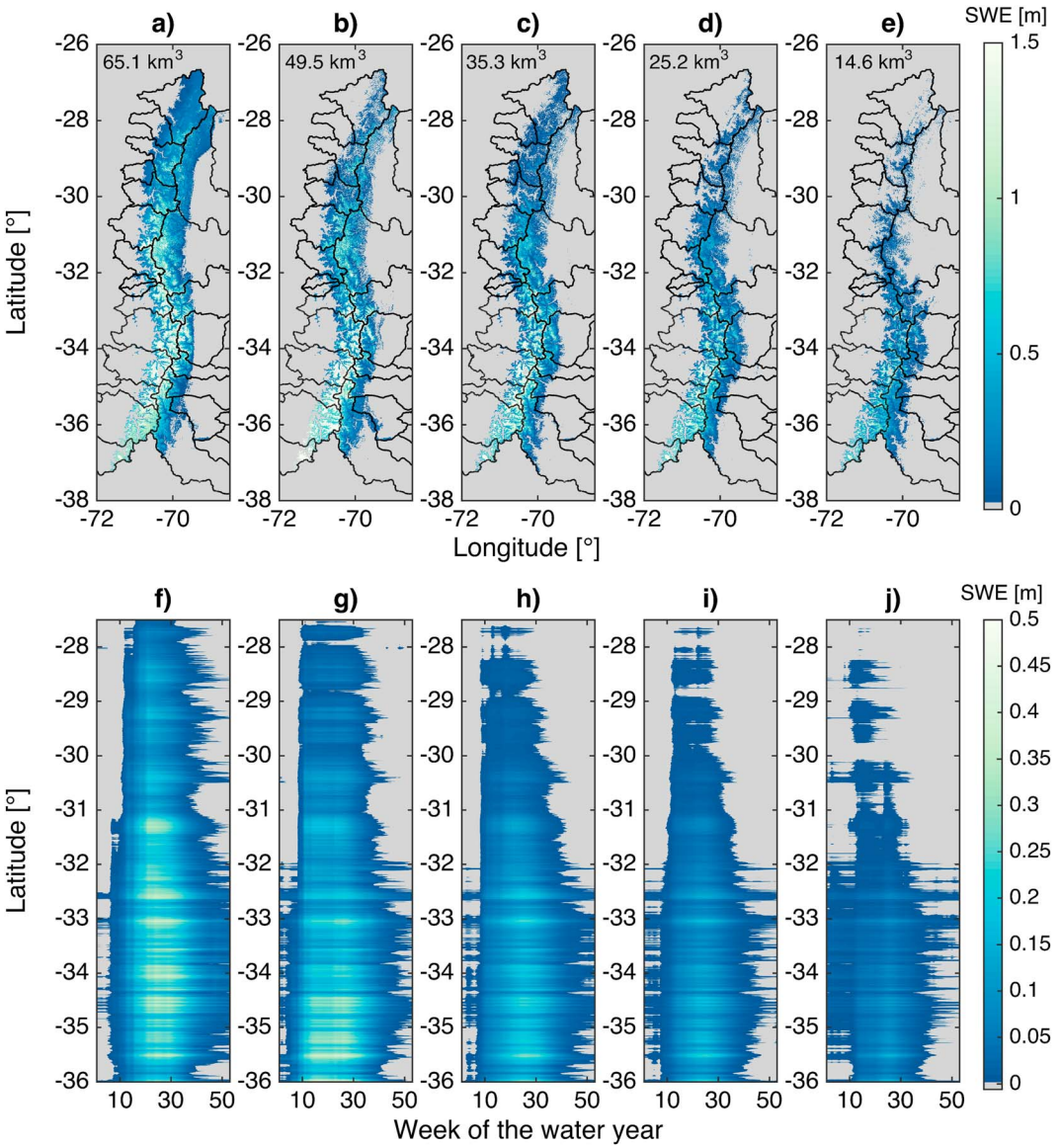

Figure 4. (a–e) Mean pixelwise peak SWE maps during El Niño and La Niña years and (f–j) Hovmöller diagrams for the average weekly SWE distribution. Very strong El Niño (Figures 4a and 4f), strong El Niño (Figures 4b and 4g), weak El Niño (Figures 4c and 4h), weak La Niña (Figures 4d and 4i), and strong La Niña (Figures 4e and 4j).

predominantly result in negative anomalies south of 31°S, although the variation of the anomaly is not as significant as the *Z* score difference seen for 1987. A detailed analysis of the presence of storms throughout the season is required in order to understand the underlying reasons behind the spatial variability in ONI-driven anomalies.

Figure 5c shows the latitudinal variation of the correlation coefficient between the annual time series of domain-averaged peak SWE and ONI. Spearman (rank-based) correlation coefficients were included since rank-based correlations are more robust to outliers. The 1987 and 1997 El Niño years influence the Pearson correlation coefficient significantly for the Northern regions due to the high SWE accumulations, resulting in deceivingly high correlation coefficients north of 31°S. Regions south of 33°S tend to show a lower number of extreme years (i.e., no significant *Z* score deviation), and hence the Pearson and Spearman correlation coefficients tend to converge. Based on these results, the region with the largest influence by ENSO variations is the 33°S to 35°S latitude range, with a mean correlation of approximately 0.5 using both Pearson and Spearman calculations.

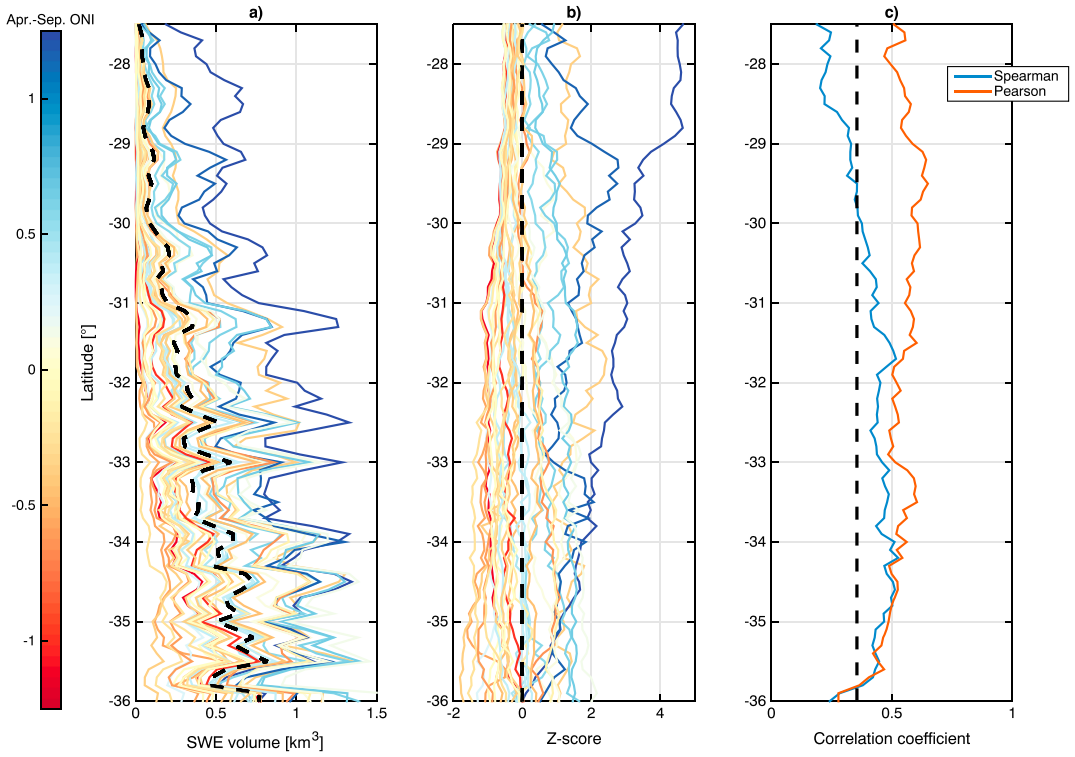

Figure 5. Relationship between latitudinal SWE distribution and ONI. (a) Annual SWE volume averaged over 0.1° latitude intervals; (b) annual *Z* score of the SWE volume averaged over 0.1° latitude intervals; and (c) correlation coefficient between the annual *Z* score and the April to September ONI index. For Figures 5a and 5b the black dashed line shows the 31 year climatology of SWE and the *Z* score line, respectively, while for Figure 5c it shows the value for the correlation coefficient that corresponds to a significance level of 95%.

4. Conclusions

This paper presents a new high-resolution snowpack data set generated by integrating ensemble simulations and remotely sensed observations of snow covered area from the Landsat satellites. The data set illustrates how snow over the Andes shows significant latitudinal variability in accordance with the significant climatic and topographic variability across the domain. Northern watersheds are characterized by low peak SWE values due to the high aridity and the low number of storms carrying significant precipitation. During the 1987 and 1997 El Niño years these watersheds experienced significant positive anomalies, and some of the watersheds evaluated in this study show that only 2 or 3 years are responsible for up to 80% of the total cumulative SWE observed over the entire time series. The extreme effect of these El Niño years in snow accumulation, particularly over the northern regions, together with the prevalence of snow-drought conditions for the region hints at a greater need to evaluate the effect of El Niño in phenomena that are directly impacted by snow precipitation such as glacier mass balance and seasonal runoff. Southern watersheds show a more stable climatological regime with a more uniform distribution of snow volumes across the record, and a more limited impact of El Niño on snow accumulation, although the ONI index still shows a correlation with SWE volumes for these latitudes. The high temporal variability exhibited in the northern regions represents an interesting challenge for water planners, as aridity is the norm and the climatological mean may be significantly affected by the presence of strong El Niño years in the time series. The impact of El Niño events in 1987 and 1997 on snow deserve further study given the significant positive SWE anomalies observed throughout the domain, particularly for the regions north of 33°S.

Acknowledgments
Funding was provided by a PhD fellowship (Chilean government Becas Chile program) and a NASA NEWS project (grant NNX15AD16G). Snow survey data were provided by James McPhee of Universidad de Chile. MERRA data are available for free at http://gmao.gsfc.nasa.gov/research/merra/. Landsat data are available for free at http://earthexplorer.usgs.gov/. This work used computational and storage services associated with the Hoffman2 Shared Cluster provided by UCLA IDRE Research Technology Group. The data used in this work are available at http://aqua.seas.ucla.edu/data.

References

Boisier, J. P., R. Rondanelli, R. D. Garreaud, and F. Muñoz (2016), Anthropogenic and natural contributions to the Southeast Pacific precipitation decline and recent megadrought in central Chile, *Geophys. Res. Lett.*, *43*, 413–421, doi:10.1002/2015GL067265.

Cornwell, E., N. P. Molotch, and J. McPhee (2016), Spatio-temporal variability of snow water equivalent in the extra-tropical Andes Cordillera from distributed energy balance modeling and remotely sensed snow cover, *Hydrol. Earth Syst. Sci.*, *20*, 411–430, doi:10.5194/hess-20-411-2016.

Cortés, G., M. Girotto, and S. A. Margulis (2014), Analysis of sub-pixel snow and ice extent over the extratropical Andes using spectral unmixing of historical Landsat imagery, *Remote Sens. Environ.*, *141*, 64–78, doi:10.1016/j.rse.2013.10.023.

Cortés, G., M. Girotto, and S. Margulis (2016), Snow process estimation over the extratropical Andes using a data assimilation framework integrating MERRA data and Landsat imagery, *Water Resour. Res.*, *52*, 2582–2600, doi:10.1002/2015WR018376.

Cosgrove, B. A., et al. (2003), Land surface model spin-up behavior in the North American Land Data Assimilation System (NLDAS), *J. Geophys. Res.*, *108*(D22), 8845, doi:10.1029/2002JD003316.

Dozier, J., E. H. Bair, and R. E. Davis (2016), Estimating the spatial distribution of snow water equivalent in the world's mountains, *Wiley Interdiscip. Rev.: Water*, *3*(3), 461–474, doi:10.1002/wat2.1140.

Garreaud, R. D. (2009), The Andes climate and weather, *Adv. Geosci.*, *22*(22), 3–11.

Girotto, M., S. A. Margulis, and M. Durand (2014), Probabilistic SWE reanalysis as a generalization of deterministic SWE reconstruction techniques, *Hydrol. Process.*, *28*(12), 3875–3895, doi:10.1002/hyp.9887.

Kaufman, L., and P. J. Rousseeuw (2009), *Finding Groups in Data: An Introduction to Cluster Analysis*, vol. 344, pp. 1–68, John Wiley, New York.

Kunkel, K. E. (1989), Simple procedures for extrapolation of humidity variables in the mountainous western United States, *J. Clim.*, *2*(7), 656–669, doi:10.1175/1520-0442(1989)002<0656:SPFEOH>2.0.CO;2.

Liston, G. E. (2004), Representing subgrid snow cover heterogeneities in regional and global models, *J. Clim.*, *17*(6), 1381–1397, doi:10.1175/1520-0442(2004)017<1381:RSSCHI>2.0.CO;2.

Liston, G. E., and K. Elder (2006), A meteorological distribution system for high-resolution terrestrial modeling (MicroMet), *J. Hydrometeorol.*, *7*(2), 217–234, doi:10.1175/JHM486.1.

Margulis, S. A., M. Girotto, G. Cortés, and M. Durand (2015), A particle batch smoother approach to snow water equivalent estimation, *J. Hydrometeorol.*, *16*(4), 1752–1772, doi:10.1175/JHM-D-14-0177.1.

Margulis, S. A., G. Cortés, M. Girotto, and M. Durand (2016a), A Landsat-era Sierra Nevada (USA) snow reanalysis (1985–2015), *J. Hydrometeorol.*, doi:10.1175/JHM-D-15-0177.1.

Margulis, S. A., G. Cortés, M. Girotto, L. S. Huning, D. Li, and M. Durand (2016b), Characterizing the extreme 2015 snowpack deficit in the Sierra Nevada (USA) and the implications for drought recovery, *Geophys. Res. Lett.*, *43*, 6341–6349, doi:10.1002/2016GL068520.

Masiokas, M. H., R. Villalba, B. H. Luckman, C. Le Quesne, and J. C. Aravena (2006), Snowpack variations in the central Andes of Argentina and Chile, 1951–2005: Large-scale atmospheric influences and implications for water resources in the region, *J. Clim.*, *19*(24), 6334–6352, doi:10.1175/JCLI3969.1.

Mernild, S. H., G. E. Liston, C. A. Hiemstra, J. K. Malmros, J. C. Yde, and J. McPhee (2016), The Andes Cordillera. Part I: Snow distribution, properties, and trends (1979–2014), *Int. J. Climatol.*, *37*, 1680–1698, doi:10.1002/joc.4804.

Montecinos, A., A. Díaz, and P. Aceituno (2000), Seasonal diagnostic and predictability of rainfall in subtropical South America based on tropical Pacific SST, *J. Clim.*, *13*(4), 746–758, doi:10.1175/1520-0442(2000)013<0746:SDAPOR>2.0.CO;2.

Pan, M., et al. (2003), Snow process modeling in the North American Land Data Assimilation System (NLDAS): 2. Evaluation of model simulated snow water equivalent, *J. Geophys. Res.*, *108*(D22), 8850, doi:10.1029/2003JD003994.

Painter, T. H., J. Dozier, D. A. Roberts, R. E. Davis, and R. O. Green (2003), Retrieval of subpixel snow-covered area and grain size from imaging spectrometer data, *Remote Sens. Environ.*, *85*(1), 64–77, doi:10.1016/S0034-4257(02)00187-6.

Rienecker, M. M., et al. (2011), MERRA: NASA's modern-era retrospective analysis for research and applications, *J. Clim.*, *24*, 3624–3648, doi:10.1175/JCLI-D-11-00015.1.

Rittger, K., T. H. Painter, and J. Dozier (2013), Assessment of methods for mapping snow cover from MODIS, *Adv. Water Resour.*, *51*, 367–380, doi:10.1016/j.advwatres.2012.03.002.

Rubio-Álvarez, E., and J. McPhee (2010), Patterns of spatial and temporal variability in streamflow records in south central Chile in the period 1952–2003, *Water Resour. Res.*, *46*, W05514, doi:10.1029/2009WR007982.

Urrutia, R., and M. Vuille (2009), Climate change projections for the tropical Andes using a regional climate model: Temperature and precipitation simulations for the end of the 21st century, *J. Geophys. Res.*, *114*, D02108, doi:10.1029/2008JD011021.

Xue Y., S. Sun, D. S. Kahan, and Y. Jiao (2003), Impact of parameterizations in snow physics and interface processes on the simulation of snow cover and runoff at several cold region sites, *J. Geophys. Res.*, *108*(D22), 8859, doi:10.1029/2002JD003174.

Yang, Z. L., R. E. Dickinson, A. Robock, and K. Y. Vinnikov (1997), Validation of the snow submodel of the biosphere-atmosphere transfer scheme with Russian snow cover and meteorological observational data, *J. Clim.*, *10*(2), 353–373, doi:10.1175/1520-0442(1997)010<0353:VOTSSO>2.0.CO;2.

Yi, Y., J. S. Kimball, L. A. Jones, R. H. Reichle, and K. C. McDonald (2011), Evaluation of MERRA land surface estimates in preparation for the soil moisture active passive mission, *J. Clim.*, *24*(15), 3797–3816, doi:10.1175/2011JCLI4034.1.

Viale, M., and M. N. Nuñez (2011), Climatology of winter orographic precipitation over the subtropical central Andes and associated synoptic and regional characteristics, *J. Hydrometeorol.*, *12*(4), 481–507, doi:10.1175/2010JHM1284.1.